arXiv:1403.2859v1 [cond-mat.str-el] 12 Mar 2014

μSR and inelastic neutron scattering investigations of the noncentrosymmetric antiferromagnet $CeNiC_2$

A.Bhattacharyya[1,2],* D.T. Adroja[1,2],† A.M. Strydom[2], A. D . Hillier[1], J.W. Taylor[1], A. Thamizhavel[3], S. K. Dhar[3], W. A. Kockelmann[1], and B. D. Rainford[4]
[1]*ISIS Facility, Rutherford Appleton Laboratory, Chilton, Didcot Oxon, OX11 0QX, UK*
[2]*Physics Department, University of Johannesburg, PO Box 524, Auckland Park 2006, South Africa*
[3] *Tata Institute of Fundamental Research, Homi Bhabha Road, Colaba, Mumbai 400005, India and*
[4]*Department of Physics, Southampton University, Southampton S09 5NH , United Kingdom*
(Dated: March 13, 2014)

The magnetic state of the noncentrosymmetric antiferromagnet $CeNiC_2$ has been studied by magnetic susceptibility, heat capacity, muon spin relaxation (μSR) and inelastic neutron scattering (INS) measurements. $CeNiC_2$ exhibits three magnetic phase transitions at T_{N_1} = 20 K, T_{N_2} = 10 K and T_{N_3} = 2.5 K. The presence of long range magnetic order below 20 K is confirmed by the observation of oscillations in the μSR spectra between 10 and 20 K and a sharp increase in the muon depolarization rate. INS studies reveal two well-defined crystal electric field (CEF) excitations around 8 and 30 meV. INS data have been analyzed using a CEF model and the wave functions were evaluated. We also calculated the direction and magnitude of the ground state moment using CEF wave functions and compare the results with that proposed from the neutron diffraction. Our CEF model correctly predicts that the moments order along the $b-$axis (or y-axis) and the observed magnetic moment is 0.687(5) μ_B, which is higher than the moment observed from the neutron diffraction (0.25 μ_B/Ce). We attribute the observed reduced moment due to the Kondo screening effect.

PACS numbers: 75.10.Dg, 75.30.Gw, 75.30.Mb, 75.20.Hr

I. INTRODUCTION

A rich variety of novel phenomena perceptible in Ce-based strongly correlated electron systems due to the duality between the localized and the itinerant nature of f-electrons, such as heavy electron and mixed valence behavior, Kondo insulator or semiconductors, unconventional superconductivity, spin and charge density waves, spin and charge gap formation and metal-insulator transition of special recent interest, is the fascinating phenomena associated with magnetic quantum criticality and non-Fermi liquid behavior arising from cooperative behavior at a zero temperature phase transition.[1–7]

$RNiC_2$ (R = rare earth) compounds crystallize in the noncentrosymmetric (NCS) orthorhombic $CeNiC_2$ type structure (space group Amm2) in which a mirror plane is missing along the c-axis.[8] Diverse ground states such as the superconducting, antiferromagnetic (AFM)/ferromagnetic (FM) and the charge density-wave (CDW) state are reported so far in $RNiC_2$(R = La, Ce, Pr, Sm, Gd, Tb and Er), reflecting the competition among different electronic states.[8–11] No structural phase transition has been reported in these compounds, and hence the spin and charge ordering phenomena in $RNiC_2$ compounds are thus native to the NCS crystal structure. $LaNiC_2$ is a superconductor below about 2.7 K.[12,13] The absence of an inversion center is believed to give rise to mixed wave pair states (s-wave singlet and p-wave triplet) in NCS superconductors. It has been argued that heavy fermion effects are not significant except perhaps for R = Ce (perhaps mixed valence effects for Sm). Murase et al [11] found that rare-earth intermetallic compounds $RNiC_2$ with R = Nd, Sm, Gd and Tb show anomalous temperature dependences of electrical resistivity and lattice constants.[11] They proposed that these anomalies are attributed to CDW transitions. X-

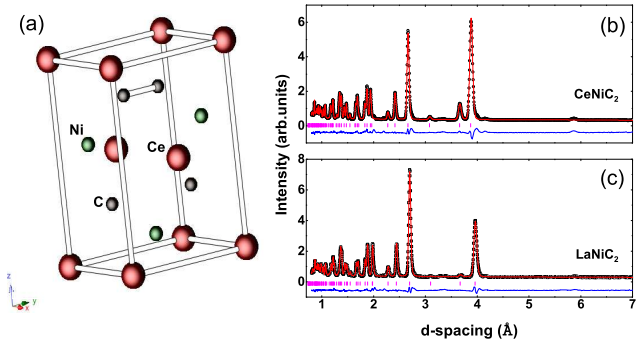

FIG. 1: (Color online) (a) The orthorhombic crystal structure of $CeNiC_2$ where the Ce atoms are in red, the Ni atoms are in green, and the C atoms are in black. (b) and (c) show the Rietveld refinement of the neutron powder diffraction pattern of $CeNiC_2$ and $LaNiC_2$ at 300 K. The data are shown as black circles, and the result of the refinement as solid lines (red).

*Electronic address: amitava.bhattacharyya@stfc.ac.uk
†Electronic address: devashibhai.adroja@stfc.ac.uk

TABLE I: A summary of the results obtained from the refinement of the room-temperature neutron powder diffraction data: the lattice parameters and atomic positions. The site occupancy for all the atoms was fixed to 100 %. The reliability factors (weighted profile factor R_{wp} = 5 %) were calculated by comparing the fit to the data (space group no. 38, Amm2).

		a (Å)	b (Å)	c (Å)
$CeNiC_2$		3.876(2)	4.548(2)	6.161(1)
$LaNiC_2$		3.957(2)	4.561(1)	6.199(2)
Atom	site	x	y	z
Ce	2a	0.00	0.00	1.00
Ni	2b	0.500	0.00	0.6138(2)
C	4e	0.500	0.3509(2)	0.8043(1)
La	2a	0.00	0.00	1.00
Ni	2b	0.500	0.00	0.6137(1)
C	4e	0.500	0.3513(1)	0.8047(2)

ray scattering studies of $SmNiC_2$ reveal satellite peaks corresponding to an incommensurate wave vector (0.5, 0.52, 0) below 148 K at which the resistivity shows an anomaly, signing development of a charge-density wave.[14] The rare earth local moments order antiferromagnetically in most of the $RNiC_2$ compounds (apart from R = Pr), and $SmNiC_2$ undergoes a first-order ferromagnetic transition at T_C = 17.5 K.[14] Those results indicate that $RNiC_2$ compounds having various magnetic orders are promising candidates for the systematic investigation of the interplay of CDW and magnetic order. In this system, nickel atoms are nonmagnetic and rare-earth elements mainly contribute to the magnetic properties showing the character of local magnetic moments interacting through the Ruderman−Kittel−Kasuya−Yosida (RKKY) interaction. The magnetic properties of the $RNiC_2$ series are affected strongly by the orthorhombic crystalline electric field (CEF).

In this paper we report a detailed investigation on $CeNiC_2$ by dc magnetic susceptibility (χ), isothermal magnetization (M), heat capacity (C_P), neutron diffraction, muon spin relaxation (μSR) and inelastic neutron scattering (INS) measurements. Below 20 K a sharp anomaly is observed in our $\chi(T)$ and C_P data which corresponds to a transition from the paramagnetic (PM) to AFM state. $C_P(T)$ data also show a second anomaly around 2.5 K and a further weak anomaly near 10 K. The presence of long-range magnetic order is also revealed by μSR measurements where oscillations are observed in the spectra below 20 K. A doublet ground state is inferred both from $C_P(T)$ and INS data. INS reveals two well-defined CEF excitations at 9 and 28 meV, indicating the localized nature of the $4f-$electrons in $CeNiC_2$.

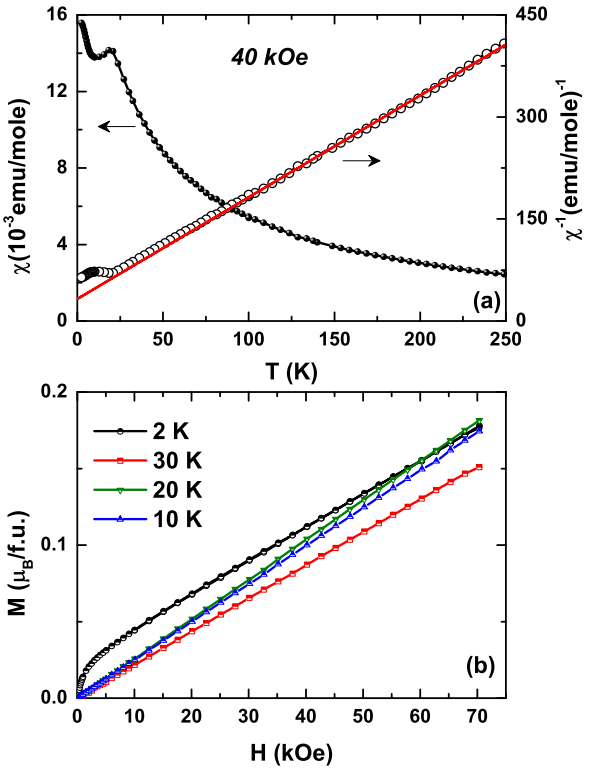

FIG. 2: (Color online) (a) Temperature dependence of the magnetic susceptibility and the inverse $\chi(T)$ of polycrystalline $CeNiC_2$. The straight lines show fits to CW behavior in the high-temperature region. (b) Isothermal field dependence of magnetization at different constant temperatures.

II. EXPERIMENTAL DETAILS

Polycrystalline samples of $CeNiC_2$ and $LaNiC_2$ were prepared by arc-melting of the constituent elements (Ce : 99.999 wt.-%, La : 99.999 wt.-%, Ni : 99.999 wt.-%, C : 99.999 wt.-%) in an argon atmosphere on a water cooled copper hearth. After being flipped and remelted several times, the buttons were wrapped in tantalum foil and annealed at 1000 ^{0} C for 168 h under a dynamic vacuum, better than 10^{-6} Torr. Powder X-ray diffraction measurements were carried out using a Panalytical X-Pert Pro diffractometer. Magnetic susceptibility measurements were made using a MPMS SQUID magnetometer (Quantum Design). Heat capacity measurements were performed by the relaxation method in a Quantum Design physical properties measurement system (PPMS).

The muon spin relaxation and inelastic neutron scattering experiments were carried out at the ISIS Pulsed Neutron and Muon Facility of the Rutherford Appleton Laboratory, United Kingdom. To check the phase purity of the samples room temperature neutron diffraction measurements were carried out using General Ma-

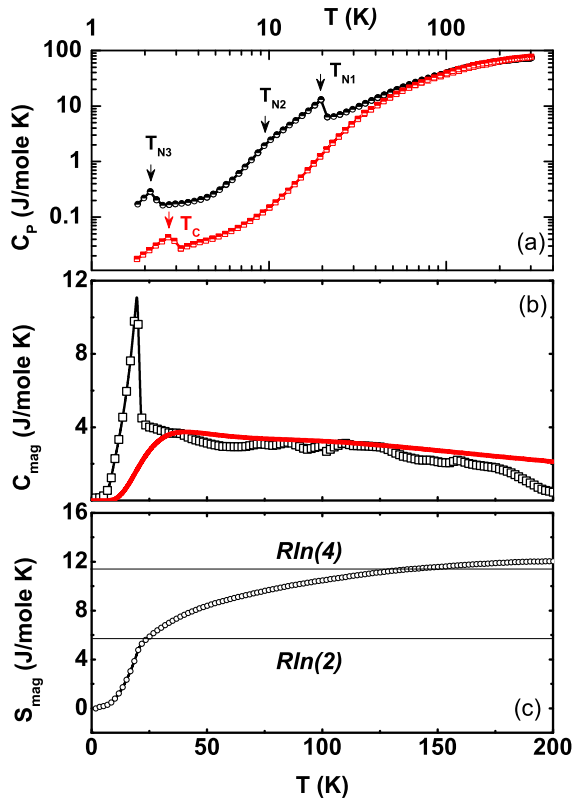

FIG. 3: (Color online) (a) Temperature dependence of the heat capacity of $CeNiC_2$ (black circle) and the phonon reference compound $LaNiC_2$ (red square) (b) Estimated magnetic contribution of the heat capacity plotted as C_{mag} vs. T and the red curve represents the crystal electric field contribution to specific heat according to the crystal field level scheme deduced from the inelastic neutron scattering data (c) The temperature-dependent magnetic entropy estimated from the experimental data in (b).

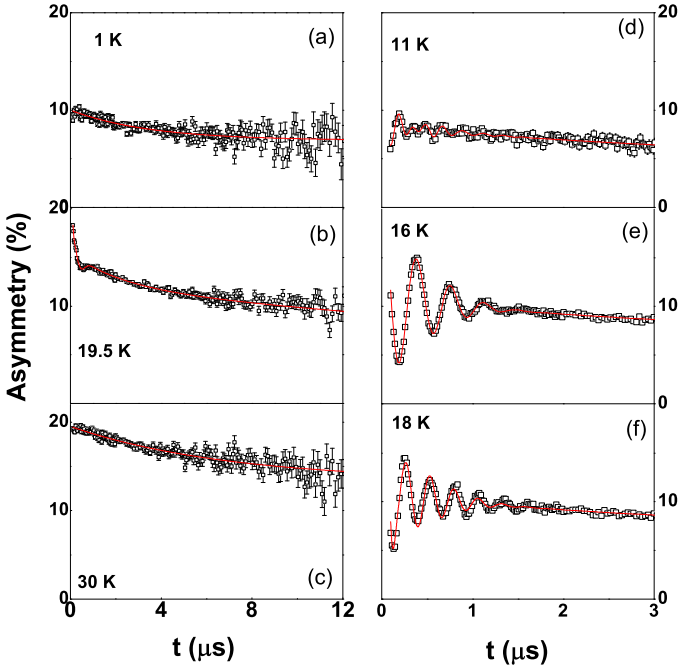

FIG. 4: (Color online) Zero-field μSR spectra plotted as asymmetry versus time at various temperatures of $CeNiC_2$. The solid lines depict fits using Eq. (1) (see text).

terials (GEM) time of flight (TOF) diffractometer. The INS measurements were carried out on the time-of-flight MARI spectrometer between 5 and 100 K. The powder samples were wrapped in thin Al foil and mounted inside a thin-walled cylindrical Al can, which was cooled down to 4.5 K inside a top-loading closed cycle refrigerator with helium exchange gas around the sample. Incident neutron energies (E_i) of 8, 20 and 50 meV were used on MARI selected via a Gd-Fermi chopper. The μSR measurement was carried out on the MUSR spectrometer with the detectors in a longitudinal configuration. The powdered sample was mounted on a high purity silver plate using diluted GE varnish and covered with kapton film which was cooled down to 1.2 K in a standard ^{4}He cryostat with He-exchange gas. Spin-polarized muon pulses were implanted into the sample and positrons from the resulting decay were collected in positions either forward or backwards of the initial muon spin direction. The asymmetry is calculated by, $G_z(t) = [N_F(t) - \alpha N_B(t)]/[N_F(t) + \alpha N_B(t)]$, where $N_B(t)$ and $N_F(t)$ are the number of counts at the detectors in the forward and backward positions and α is a constant determined from calibration measurements made in the paramagnetic state with a small (20 G) applied transverse magnetic field.

III. RESULTS AND DISCUSSION

A. Room temperature Neutron diffraction

Powder neutron diffraction measurements were carried out at room temperature on the polycrystalline $RNiC_2$ (R = Ce and La) samples. Rietveld refinement was carried out using the GSAS software on the basis of orthorhombic $CeNiC_2$ type crystal structure (Space group No. 38).[15] In this structure Ce/La atom occupies 2a sites, Ni atom 2b sites and C atom 4e sites. Rietveld refinement profile along with neutron diffraction patterns of these compounds are shown in Figs. 1 (b)-(c). One small impurity peak was detectable in $CeNiC_2$ (1% of the intensity of the maximum sample peak) whilst none were observed in $LaNiC_2$, indicating that the samples are single phase. The site occupancies were all fixed at 100%. The results of the refinements are displayed in Table I. Observed lattice parameters are in agreement with the previously reported values.[15] The nearest-neighbor

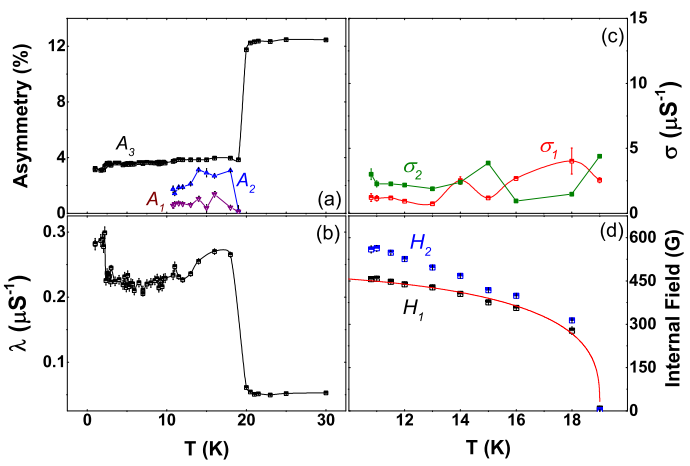

FIG. 5: (Color online) The temperature dependence of (a) the initial asymmetries A_1, A_2 and A_3 (b) the depolarization rate λ, (c) the depolarization rates σ_1 and σ_2, and (d) the internal fields H_1 and H_2. The solid line in (d) is fit to Eq. 2 (see text).

distances are 3.8305 Å for Ce-Ce, 3.0671 Å for Ce-Ni, 1.9687 Å for Ni-C.

B. Magnetization and Heat capacity

The temperature (T) variation of the dc magnetic susceptibility ($\chi = M/H$, where H is the applied magnetic field) measured in zero field cooled condition in $H = 40$ kOe is shown in Fig. 2 (a). χ shows a drop below 20 K with decreasing T. This corresponds to the PM/AFM transition (T_{N_1}) in the sample. The magnetic susceptibility of $CeNiC_2$ above 50 K exhibits Curie-Weiss behavior. A linear least-squares fit yields an effective magnetic moment p_{eff}= 2.30 μ_B, which is close to free Ce^{3+}-ion value (2.54 μ_B), and a negative paramagnetic Curie temperature θ_p= −15 K. The value of magnetic moment suggests that the Ce atoms are in their normal Ce^{3+} valence state, which agrees with smooth variation of the unit cell volume in $RNiC_2$ series.[15] Negative value of θ_p is indicative of a negative exchange constant and AFM ordering. $LaNiC_2$ shows weak Pauli paramagnetism type behavior (not shown here, which confirms that Ni is nonmagnetic in $RNiC_2$ series).[16]

Fig. 2 (b) shows the M versus H isotherms recorded at different temperatures. $M - H$ data imply that the net magnetization in the ordered state of $CeNiC_2$ is extremely low. It is far from saturation and barely reaches 7% of that expected theoretically gJ= 2.14 μ_B for Ce^{3+} ions, in a 70 kOe magnetic field. This is consistent with previously reported results.[9,10] The low values of the observed magnetization is expected for an AFM ground state due to the cancellation of magnetization from different magnetic sublattices of Ce ions.

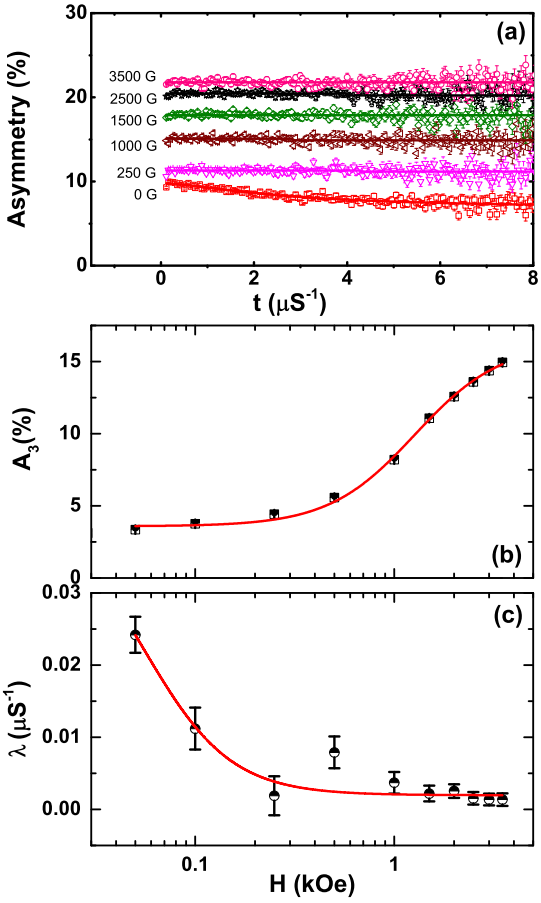

FIG. 6: (Color online) (a) Field dependent μSR spectra at 1.2 K . (b) the longitudinal component of the initial asymmetry (A_3) and depolarization rate (λ) as a function of applied magnetic field at 1.2 K. The solid lines represent fits to Eq. (3) and Eq. (4) respectively.

Zero field C_P versus T data of both compounds from 2 to 300 K are shown in Fig. 3 (a). For $LaNiC_2$, $C_P(T)$ data show sharp discontinuity between 2 and 3 K which is consistent with the transition to the superconducting state. The discontinuity in the heat capacity of $LaNiC_2$, $\Delta C/\gamma T_C$ = 1.20, suggests weak electron-electron coupling and confirms the bulk nature of superconductivity.[16] For $CeNiC_2$ a clear signature of anomaly is observed at T_{N_1} = 20 K and T_{N_3} = 2.5 K and a further weak anomaly is observed at T_{N_2} = 10 K which matches well with previous reports.[16] We have carefully looked at low T behavior of C_P. At $T \ll \Theta_D$ (Θ_D = Debye temperature), the lattice part of the heat capacity C_{debye} has a T^3 dependence. We estimate γ and Θ_D using same method as reported by V. K. Pecharsky et.al.[16] and find similar values of γ (6.0 mJ mol^{-1} K^{-2}) and Θ_D (380 K).

The magnetic contribution to the specific heat C_{mag} is shown in Fig. 3 (b). The C_{mag} was estimated by subtracting off the lattice contribution equal to the specific

heat of isostructural $LaNiC_2$. The effect of crystal electric field is reflected as a broad Schottky-type anomaly centered around 52 K in C_{mag}. The solid curve in Fig. 3(b) represents the crystal field contribution to specific heat according to the CEF level scheme obtained from the analysis of inelastic neutron scattering data. The magnetic contribution to entropy S_{mag} was obtained by integrating the $C_{mag}(T)/T$ versus T plot and is shown in Fig. 3(c). A value of S_{mag} around the magnetic ordering temperature is comparable with $Rln2$ suggesting a CEF split doublet ground state in $CeNiC_2$ and is confirmed by the INS data in section D.

C. Muon spin relaxation

The time dependence of asymmetry (μSR) spectra of $CeNiC_2$ measured at various temperatures in zero field are shown in Figs. 4 (a)-(f). The spectra show exponential type decay above 20 K in the paramagnetic state. In the temperature range 10 K $\leq T \leq$ 20 K, muon spin precession with two frequencies is observed, indicating that at least two muon sites exist in the compound. Below 10 K, as shown in Fig. 4 (a), muon spin precession is not observable due to the fact that internal fields exceed the maximum internal field detectable on the μSR spectrometer due to the pulse width of the ISIS muon beam. In between these temperature ranges 2 K $\leq T \leq$ 10 and 20 K $\leq T \leq$ 30 K, we used simple exponential decay plus constant background to fit our μSR spectra. In the range 10 K $\leq T \leq$ 20 K, the spectra were fitted with,[17,18]

$$G_z(t) = \sum_{i=1}^{n} A_i cos(\gamma_\mu H_i t + \phi) e^{-\frac{\sigma_i^2 t^2}{2}} + A_3 e^{-\lambda t} + A_{bg} \quad (1)$$

where the initial amplitude of the exponential decay and the oscillatory component are A_3 and A_i respectively, the internal magnetic fields at the muon stopping site i are H_i, the Gaussian decay rate is σ_i, λ is the muon depolarization rate, ϕ is the common phase, $\gamma_\mu/2\pi$ = 135.53 MHz T^{-1} and A_{bg} is the background. The temperature dependencies of these parameters are shown in Figs. 5 (a)-(d). At 20 K, as shown in Fig. 5 (a) there is a loss of 2/3 value of the initial asymmetry (1/3 is left) of A_3 from the high temperature value. The initial asymmetry associated with frequency terms A_1 and A_2 start to increase below this temperature (20 K) [see Fig. 5 (a)], indicating the presence of a long-range ordered state in $CeNiC_2$ which agrees with the specific heat, magnetic susceptibility and neutron diffraction data.[8–11,16] The temperature dependence of the exponential decay term is shown in Fig. 5 (b). The muon depolarization rate (λ) was found to suddenly increase at T_{N_1}, indicating a transition between the paramagnetic and ordered states. However λ shows a weak anomaly at T_{N_2} and T_{N_3} where there is a rearrangement of the spins and a change in the magnetic structure which is in agreement with the reported change in the propagation vector from the neutron diffraction study.[19] Fig. 5(c) shows the temperature dependence of the muon depolarization rate. σ_1 and σ_2 remain almost constant within the temperature range 10 K $\leq T \leq$ 20 K.

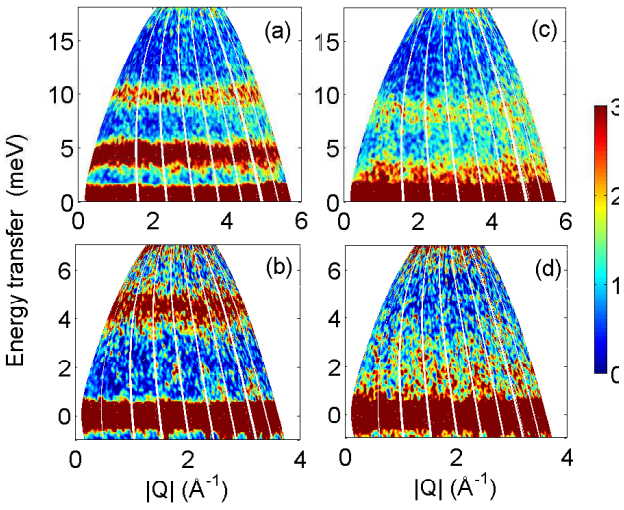

FIG. 7: (Color online) Contour plots of the inelastic scattering intensity (in mb/sr meV f.u.) plotted as energy transfer vs. wave vector transfer (Q) of $CeNiC_2$ measured with E_i = 20 meV [(a) and (c)] and 8 meV [(b) and (d)] at 5 and 25 K respectively.

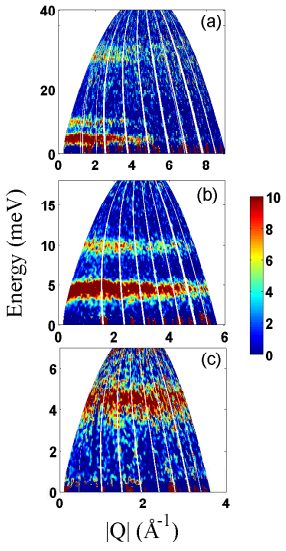

FIG. 8: (Color online) The color-coded contour map of the magnetic scattering of $CeNiC_2$ at 5 K estimated by subtracting (see text) the data of $LaNiC_2$ measured with incident energy E_i = (a) 50 meV, (b) 20 meV (c) and 8 meV respectively.

In order to find out the nature of the magnetic interaction in $CeNiC_2$ one of the two temperature dependence of internal fields was fitted with

$$H_1(T) = H_0\left(1 - \left(\frac{T}{T_N}\right)^{\alpha}\right)^{\beta} \quad (2)$$

Observed parameters are β= 0.31, H_0 = 478 G, α = 3.12 and T_N = 19.1 K (see Fig. 5 (d)). A good fit with β = 0.31 suggests the magnetic interactions in $CeNiC_2$ are 3D Ising spin system with long-range spin-spin interactions. $\alpha > 1$ indicates complex magnetic interactions in this system.

We also recorded the field dependent asymmetry spectra at 1.2 K and fitted them using an exponential function plus constant background [see Fig. 6 (a)]. Initial asymmetry (A_3) and depolarization term (λ) as a function of applied longitudinal field at 1.2 K is shown in Figs. 6 (b)-(c). The relaxation rate decreases with applied field as is conventionally expected, and we fitted the field dependence using a modified version of Redfields equation,[21]

$$\lambda = \lambda_0 + \frac{2\gamma_\mu^2\Delta^2\tau}{1+\gamma_\mu^2 H^2\tau} \quad (3)$$

where γ_μ is the muon gyromagnetic ratio, Δ describes the width of the field distribution, and τ is the characteristic timescale for the spin fluctuations experienced by the muons. The fit of $\lambda(H)$ data by Eq. (3) is shown by solid red curve in Fig. 6 (c). A good fit is obtained for λ_0= 0.002 μs^{-1}, Δ= 3.6 G, and τ_C= 20× 10^{-8} s. The observed value of τ_C in $CeNiC_2$ is comparable with $CePd_{0.15}Rh_{0.85}$.[20]

Field dependence of $A_3(H)$ (with λ as a free parameter) is shown in Fig. 6 (b). We used a quadratic-type decoupling function which is appropriate for a Lorentzian distribution of fields,[21]

$$A_3(H) = f_0 + F\frac{b^2}{1+b^2} \quad (4)$$

where the meaning of f_0, F and b (= H/H_0, H_0 internal field) parameters are given in Ref. 21.[21] A fit has been made using Eq. (4) and an internal field of 1250(40) G was obtained. The larger value of the internal field observed at 1.2 K compared to that estimated between 10 and 20 K again indicates different magnetic structures at 1.2 K and in between 10−20 K.

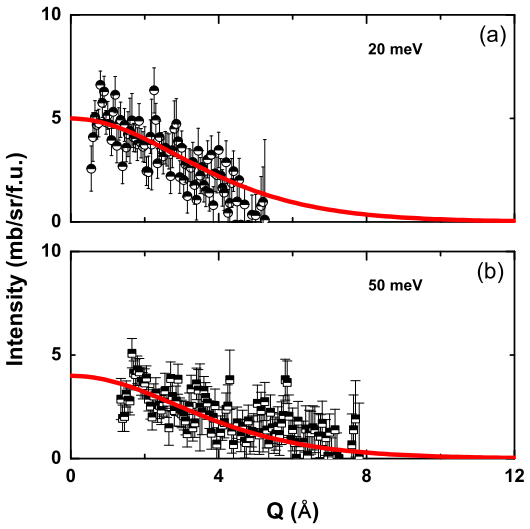

FIG. 9: (Color online) The Q dependence of total energy integrated intensity between (a) 5.85 and 11.05 meV and (b) 22 and 35 meV at 25 K for incident energy E_i =20 meV and 50 meV respectively. The solid line represents the square of the Ce^{3+} magnetic form factor (scaled to matching with the data).

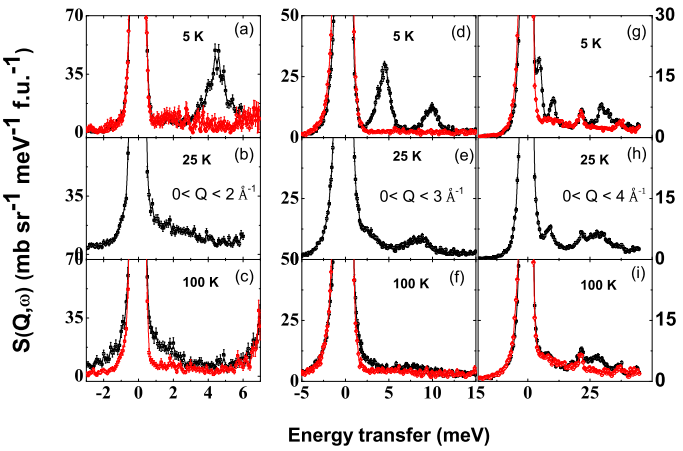

FIG. 10: (Color online) The Q-integrated 1D cuts of the total scattering from $CeNiC_2$ (black square) and $LaNiC_2$ (red circle) with an incident energy E_i = 8 meV (left panel), 20 meV (middle panel) and 50 meV (right panel) respectively.

D. Inelastic Neutron Scattering

In order to understand the origin of the reduced moment magnetism and also to investigate crystal field excitations and their energy level scheme in $CeNiC_2$ we have performed an inelastic neutron scattering study. Neutrons with incident energies E_i = 8, 20, and 50 meV were used to record the INS spectra at 5, 25, 50 and 100 K for scattering angles between 3° and 135°. The INS measurements were carried out on the polycrystalline samples of $CeNiC_2$ and $LaNiC_2$ using the MARI spectrometer. The data of $LaNiC_2$ were used to subtract the phonon contribution in $CeNiC_2$.

For magnetic neutron scattering the partial differential cross section, which measures the probability of scattering per solid angle per unit energy, is[22]

$$\frac{d^2\sigma}{d\Omega dE'} = \frac{k'}{k}\frac{N}{\hbar}(\gamma r_0)^2 F(Q)^2 \sum_{\alpha\beta}(\delta_{\alpha\beta} - \widehat{Q}_\alpha \widehat{Q}_\beta) S^{\alpha\beta(Q,\omega)} \quad (5)$$

where $k^{'}$ and k are the scattered and incident neutron wavevectors, $\gamma r_0 = 5.391$ fm is the magnetic scattering length, Q is the momentum transfer, $F(Q)$ is the magnetic form factor, ω is the energy transfer, N is the number of moments, and the summation runs over the Cartesian directions. The magnetic scattering function $S^{\alpha\beta(Q,\omega)}$ is proportional to the space and time Fourier transform of the spin-spin correlation function.[22]

To determine the correct magnetic contribution to the measured spectra, we have subtracted the phonon contribution using the data of nonmagnetic reference compound. We first used a direct subtraction method $[S(Q,\omega)_{CeNiC_2} - S(Q,\omega)_{LaNiC_2}]$ and then after allowing for a difference in the total scattering cross section $[S(Q,\omega)_{CeNiC_2} - \sigma_c \times S(Q,\omega)_{LaNiC_2}]$ (where σ_c= 0.8288 is the ratio of the total scattering cross-section of $CeNiC_2$ and $LaNiC_2$).[23,24] Both analyses gave similar magnetic response. But the second method gave slightly better estimation at low energy side in subtracting the nuclear elastic peak at zero energy transfer and hence in this paper we present all our data analyzed using the second method.

Figs. 7 (a)-(d) display the color-coded plot of the scattering intensity of energy vs. momentum transfer of $CeNiC_2$. Two inelastic excitations at 4.5 and 10 meV were observed with a significant intensity at low scattering vectors at 5 and 25 K. Absence of these excitations in $LaNiC_2$ indicates they are magnetic in origin. 5 K data has an additional magnetic excitation with a maximum at around 4.5 meV. This excitation is not present at 25 K as shown in Figs. 7 (b)-(d) where the elastic line is broadened signifying the presence of spin wave below magnetic ordering. In the paramagnetic state, the spectral weight is shifted towards the elastic line, and quasielastic scattering (QES) is observed. Figs. 8 (a)-(c) reveals the color-coded contour map of the magnetic scattering of $CeNiC_2$ at 5 K estimated by subtracting the data of $LaNiC_2$ (using second method) measured with incident energies E_i= 50 meV (a), 20 meV (b) and 8 meV (c) respectively.

Figs. 9 (a) and (b) represent the Q-dependent energy integrated intensity between (i) 5.85 and 11.05 meV , (ii) 22 and 35 meV at 25 K of $CeNiC_2$ for incident energy E_i =20 and 50 meV respectively. It follows the square of Ce^{3+} magnetic form factor $[F^2(Q)]$, which suggests that the inelastic excitations result mainly from single-ion CEF transitions. The scattering at the highest Q (not shown here) is comparable for $CeNiC_2$ and $LaNiC_2$, which indicates similar phonon contributions in these compounds. At low Q, the magnetic scattering is strong and with a small phonon contribution in $CeNiC_2$. This can be seen clearly in the 1D cuts made from the 2D color plots at low Q from 0 to 4 $Å^{-1}$ (see Fig. 10) at 5, 25 and 100 K.

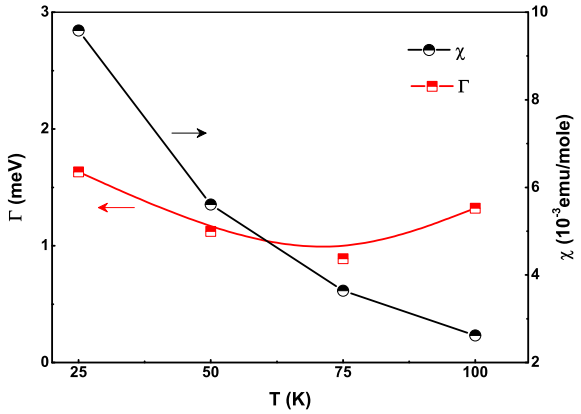

FIG. 11: (Color online) Temperature dependence of the quasielastic linewidth (left y-axis) and susceptibility (right y-axis) obtained from fitting INS data measured with an incident energy of 8 meV.

In order to estimate the quasielastic linewidth we have analyzed the 8 meV data using a Lorentzian function. We used an elastic line resolution function and an additional Lorentzian function to model the quasielastic component to fit our data. The widths of the elastic component were fixed from the measurements of vanadium with the same incident energy and frequency of the Fermi chopper. Fig. 11 (left y-axis) shows the T dependence of the half width at half maximum (HWHM, Γ). Γ doesn't change much with temperature. An estimate of the Kondo temperature (T_K) can be obtained from the value of Γ at 0 K (we used Γ value in between 50 and 80 K). For $CeNiC_2$, Γ value gives an estimation of T_K = 11 K. However at lower temperature (around 25 K) a slightly higher Γ value was observed. We attribute this to the presence of short range magnetic correlations just above T_{N_1}.

We now proceed with a more detailed analysis of the observed CEF excitations. In the orthorhombic point symmetry, Amm2 (C_{2v}), at the Ce^{3+} site and taking the z-axis as the quantization axis (i.e. $x\|a$, $y\|b$ and $z\|c$), the CEF Hamiltonian can be represented as follows:

$$H_{CEF} = B_2^0 O_2^0 + B_2^2 O_2^2 + B_4^0 O_4^0 + B_4^2 O_4^2 + B_4^4 O_4^4 \quad (6)$$

where O_n^m are the Stevens operators and B_n^m are the CEF parameters to be determined from the experimental data of inelastic neutron scattering.[25,26] The value of B_2^0 and B_2^2 can be accurately determined using the high-temperature expansion of the magnetic susceptibility,[27,28] which gives B_2^0 and B_2^2 in terms of the CW temperatures, θ_a and θ_b for an applied field parallel to a-axis

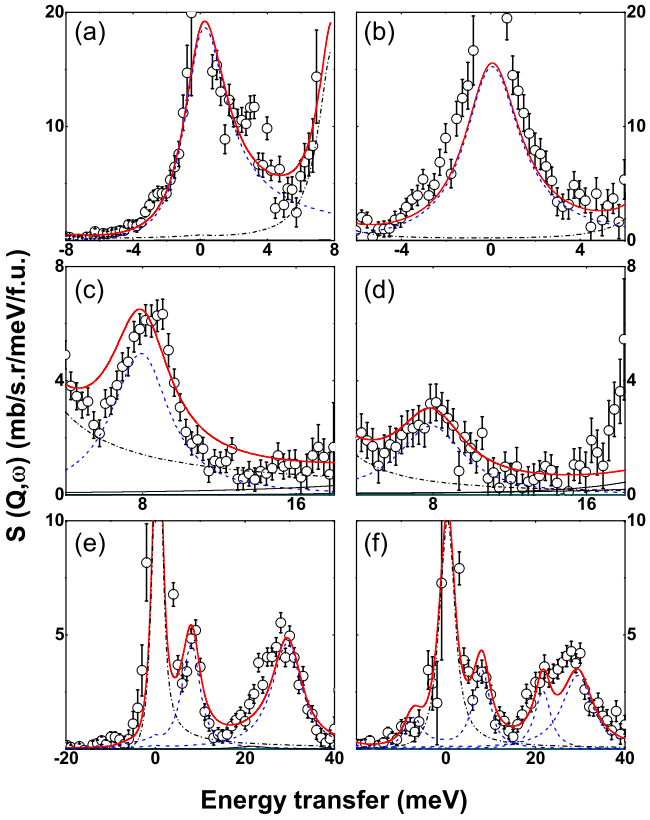

FIG. 12: (Color online) The estimated magnetic scattering of $CeNiC_2$ at 25 K (left panel) and 100 K (right panel) for momentum transfer $|Q|$ from 0 to 2 Å^{-1} for 8 meV, $|Q|$ from 0 to 3 Å^{-1} for 20 meV and $|Q|$ from 0 to 4 Å^{-1} for 50 meV. The solid lines are the fits based on the crystal electric field model and the dashed and dash-dotted lines are the components of the fit.

and b-axis, respectively and B_2^0 in terms of θ_c for an applied field parallel to c-axis. The detailed formulation have been given in ref [9]. From their formula we have determined the value of $B_2^0 = 0.08531$ meV and $B_2^2 =$ -0.8913 meV. It is to be noted that this values are valid for an isotropic exchange interaction. They were kept fixed in our initial analysis of the INS data which did not give good fit to the data and then finally we allowed to vary all five CEF parameters independently.

The solid lines in Figs. 12 (a)-(f) represent the fit to the CEF model for simultaneous refinement of all six data sets for 8, 20, and 50 meV incident energies (we first refined 25 and 100 K data). The phenomenological crystal field parameters B_n^m obtained from the best fit are given in table II.

The CEF wave functions obtained from the simultaneous fit to 25 and 100 K, INS data are given by,

TABLE II: CEF parameters B_n^m, molecular field parameters (λ_ξ , $\xi = a, b, c$) and temperature-independent constant susceptibility (χ_ξ). The parameters were estimated by simultaneous fit to the INS data at 25 K and 100K and then fitting the single-crystal susceptibility.

	25 and 100 K
B_2^0 (meV)	0.080(2)
B_2^2 (meV)	-0.650(1)
B_4^0 (meV)	-0.086(2)
B_4^2 (meV)	-0.050(3)
B_4^4 (meV)	0.209(2)
λ_a (mole/emu)	3.856
λ_b (mole/emu)	-51.214
λ_c (mole/emu)	-7.234
χ_a ($\times 10^{-3}$ emu/mole)	2.505
χ_b ($\times 10^{-3}$ emu/mole)	2.626
χ_c ($\times 10^{-3}$ emu/mole)	2.642

$$|\psi_1^{\pm}> = 0.4104|\pm\frac{5}{2}> +0.9115|\pm\frac{1}{2}> -0.0273|\pm\frac{3}{2}> \quad (7)$$

$$|\psi_2^{\pm}> = 0.8719|\pm\frac{5}{2}> -0.4010|\pm\frac{1}{2}> -0.2812|\pm\frac{3}{2}> \quad (8)$$

$$|\psi_3^{\pm}> = 0.2672|\pm\frac{5}{2}> -0.0916|\pm\frac{1}{2}> +0.9593|\pm\frac{3}{2}> \quad (9)$$

ψ_1, is the GS wave function, whereas, ψ_2 is for the first excited state at 92 K and ψ_3 is for the second excited state at 342 K above the GS. The GS magnetic moments of the Ce atoms $< \mu_x >$, $< \mu_y >$ and $< \mu_z >$, along the three crystallographic axes a, b and c, respectively can be calculated from

$$< \mu_z > = < \psi_1^{\pm} | g_J J_z | \psi_1^{\pm} > \quad (10)$$

$$< \mu_x > = < \psi_1^{\pm} | \frac{g_J}{2}(J^+ + J^-) | \psi_1^{\pm} > \quad (11)$$

$$< \mu_y > = < \psi_1^{\pm} | \frac{g_J}{2i}(J^+ - J^-) | \psi_1^{\pm} > \quad (12)$$

Calculated magnetic moments in presence of an applied magnetic field ($H = 10$ kOe; $T = 1$ K) using GS wave function are $< \mu_x > = 0.583\ \mu_B$, $< \mu_y > = 0.6876\ \mu_B$ and $< \mu_z > = 0.341\ \mu_B$. This is in agreement with neutron diffraction data, which gives possible direction of moment along $b-$axis.[19] However it is to be noted that the neutron diffraction study was unable to find accurate direction and magnitude of the moment due to limited numbers of magnetic Bragg reflections.[19]

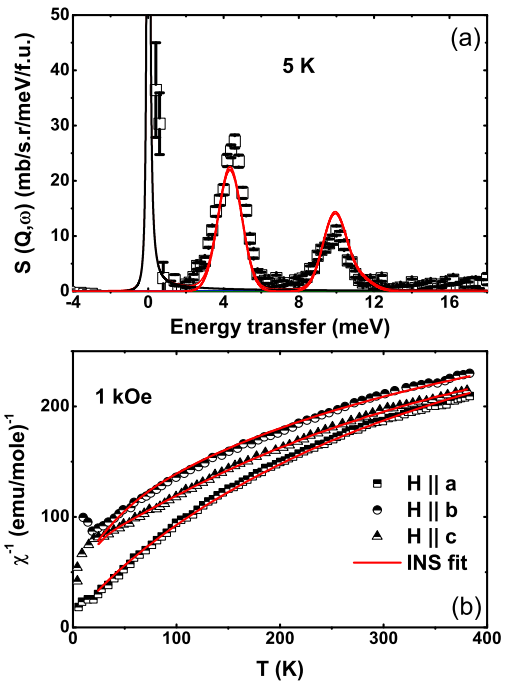

FIG. 13: (Color online) (a) The estimated magnetic scattering of $CeNiC_2$ at 5 K with E_i=20 meV. The solid line represents the fit using CEF and molecular field (see text). (b) Temperature dependence of the inverse susceptibilities along the three crystallographic axes of $CeNiC_2$. The solid line represents the fit based on the CEF model.

After obtaining CEF parameters from the simultaneous fit of the six INS data sets at 25 and 100 K, we have analyzed 20 meV INS data at 5 K (i.e. below the magnetic ordering) adding the molecular field term in the Hamiltonian. We kept the values of CEF parameters (which were obtained from 25 and 100 K as mentioned above) fixed for the analysis of 5 K data and varied molecular fields. First we varied only molecular field along $x-$axis (H_x), while keeping zero-molecular fields along $b-$ (H_y) and $c-$axes (H_z). This method did not give good fit to the data. Then we tried to vary H_y (while keeping H_x=0 and H_z=0), however we did not obtain good fit for this method either. Hence finally we varied H_x and H_y simultaneously (keeping H_z=0), which gave a reasonably good fit to the data (it is to be noted that when we also allowed to vary H_z it gave almost zero value). The values of the molecular field estimated from the analysis are H_x= 79.3(1.8) T and H_y=76.5(1.7) T. The quality of the fit can be seen in Fig. 13 (a). The presence of molecular fields along $a-$ and $b-$axes may suggests that the Ce moment is confined to the ab-plane and not along $a-$ or $b-$ axis. A detail neutron diffraction investigation using a high neutron flux instrument on $CeNiC_2$ single crystal will be helpfully to understand the presence of the molecular field along a and b-axes. To check reliability of our set of CEF parameters we model the single crystal magnetic susceptibility data from literature.[8] Observed anisotropic magnetic susceptibility data correctly fits with our calculated $\chi(T)$ using CEF parameters [see Fig. 13 (b)].

IV. CONCLUSIONS

We have studied the magnetic properties of $CeNiC_2$ using magnetic susceptibility, heat capacity, inelastic neutron scattering and μSR measurements. A magnetic transition around 20 K is observed with the emergence of oscillations in zero field μSR spectra. We fitted the temperature dependence of the internal magnetic fields to a model of a mean field magnet, which revealed 3D nature of magnetic interactions.

INS measurements of polycrystalline $CeNiC_2$ at low temperatures indicate two CEF excitations at 8 and 30 meV. At 5 K, we observe an additional peak at 4.5 meV due to spin-wave excitations. Above T_N, this peak is not present, but quasielastic scattering is observed. A linear fit to the temperature dependence of the quasielastic linewidth gives an estimate of T_K = 11 K. From an analysis of INS and magnetic susceptibility data with a CEF model, we propose a CEF scheme for $CeNiC_2$. The CEF scheme correctly predicts the direction of the ordered moment, but the observed magnetic moment at 2 K is 0.6876 μ_B/Ce which is higher compared to the moment as observed from neutron diffraction (0.25 μ_B/Ce). We believe that the observed reduced moment is due to presence of hybridization between the localized Ce^{3+} f-electrons and the conduction band. Further the susceptibility analysis reveals the anisotropic molecular fields, stronger along the b-axis, which is also in agreement with the direction of moment along the b-axis. The spin wave measurements on $CeNiC_2$ single crystal will help to shade more light on the anisotropic exchange interactions in $CeNiC_2$.

We note furthermore that the estimated on-site Kondo exchange (11 K) is of the same order of magnitude as the magnetic phase transition temperatures, which classifies this compound as a magnetically ordered Kondo lattice. The complexity of spin ordering in $CeNiC_2$ is inferred as a consequence of admixing of crystal electric field energies together with Kondo and RKKY exchange, and we believe that our study and determination of CEF parameters presented in this work establishes the essential ingredients with which to formulate an understanding of the ground state in $CeNiC_2$.

V. ACKNOWLEDGMENT

AB thanks the FRC of UJ and ISIS-STFC for funding support. DTA and ADH would like to thank CMPC-STFC, grant number CMPC-09108, for financial support. AMS thanks the SA-NRF (Grant 78832) and UJ Research Committee for financial support.

[1] A. Georges, G. Kotliar, W. Krauth, and M. J. Rozenberg, Rev. Mod. Phys. **68**, 13 (1996).

[2] C. M. Varma, Rev. Mod. Phys. **48**, 219 (1976).

[3] P. Coleman, in *Handbook of Magnetism and Advanced Magnetic Materials*, edited by H. Knoemuller and S. Parkin (Wiley, New York, 2007), Vol. **1**, p. 95.

[4] P. S. Riseborough, Adv. Phys. **49**, 257 (2000); P. S. Riseborough, Phys. Rev. B **45**, 13984 (1992).

[5] G. R. Stewart, Rev. Mod. Phys. **73**, 797 (2001); A. Amato, ibid. **69**, 1119 (1997).

[6] H. v. Lo̎hneysen, A. Rosch, M. Vojta, and P. Woelfle, Rev. Mod. Phys. **79**, 1015 (2007).

[7] A. M. Strydom, Phys. B Condens. Matter **404**, 2981 (2009).

[8] H. Onodera, Y. Koshikawa, and M. Kosaka, J. Magn. Magn. Mater. **182**, 161 (1998).

[9] K. Motoya, K. Nakaguchi, N. Kayama, K. Inari, J. Akimitsu, K. Izawa, and T. Fujita, J. Phys. Soc. Jpn. **66** 1124-1129 (1997).

[10] W. Schäfer, G. Will, J. K. Yakinthos, and P. A. Kotsanidis, J. Alloy. Compd. **180**, 251 (1992).

[11] M. Murase, A. Tobo, H. Onodera, Y. Hirano, T. Hosaka, S. Shimomura, and N. Wakabayashi, J. Phys. Soc. Jap. **73**, 2790 (2004).

[12] W.H. Lee, H.K. Zeng, Y.D. Yao, and Y.Y. Chen, Physica C **266**, 138 (1996).J. Quintanilla

[13] A. D. Hillier, J. Quintanilla, and R. Cywinski, Phys. Rev. Lett. **102**, 117007 (2009).

[14] S. Shimomura, C. Hayashi, G. Asaka, N. Wakabayashi, M. Mizumaki, and H. Onodera, Phys. Rev. Lett. **102**, 076404 (2009).

[15] P. Kotsanidis, J. K. Yakinthos, and E. Gamari-Seale, J. Less. Comm. Met. **152**, 287 (1989).

[16] V. K. Pecharsky, L. L. Miller, and K. A. Gschneidner, Jr., Phys. Rev. B **58**, 497 (1998).

[17] M. Smidman, D. T. Adroja, A. D. Hillier, L. C. Chapon, J. W. Taylor, V. K. Anand, R. P. Singh, M. R. Lees, E. A. Goremychkin, M. M. Koza, V. V. Krishnamurthy, D. M. Paul, and G. Balakrishnan, Phys. Rev. B **88**, 134416 (2013).

[18] A. D. Hillier, D. T. Adroja, P. Manuel, V. K. Anand, J. W. Taylor, K. A. McEwen, B. D. Rainford, and M. M. Koza, Phys. Rev. B **85**, 134405 (2012).

[19] K. Motoya, K. Nakaguchi, N. Kayama, K. Inari, J. Akimitsu, K. Izawa, and T. Fujita, J. Phys. Soc. Jpn. **66**, 1124 (1997).

[20] D.T. Adroja, A.D. Hillier, J.-G. Park, W. Kockelmann, K.A. McEwen, B.D. Rainford, K.-H. Jang, C. Geibel, and T. Takabatake, Phys. Rev. B **78**, 014412 (2008).

[21] S. M. Disseler, C. Dhital, A. Amato, S. R. Giblin, C. de la Cruz, S. D. Wilson, and M. J. Graf, Phys. Rev. B **86**, 014428 (2012).

[22] S. Lovesey, *Theory of Neutron Scattering from Condensed Matter*, (Oxford University Press, Oxford, UK, 1984).

[23] V. K. Anand, D. T. Adroja, A. D. Hillier, J. Taylor, and G. André, Phys. Rev. B **84**, 064440 (2011).

[24] D. T. Adroja and V. K. Anand, Phys. Rev. B **86**, 104404 (2012).

[25] K. Stevens, Proc. Phys. Soc. Sect. A **65**, 209 (1952).

[26] K. Stevens, Rept. Progr. Phys. **30**, 189 (1967).

[27] J. Jensen and A. R.Mackintosh, *Rare Earth Magnetism*, (Clarendon Press, Oxford, 1991).

[28] Y. Koshikawa, H. Onodera, M. Kosaka, H. Yamauchi, M. Ohashi, and Y. Yamaguchi, J. Magn. Magn. Mater. **173**, 72-82 (1997).